

## Disease-Modifying Anti-Alzheimer's Drugs: Inhibitors of Human Cholinesterases Interfering with $\beta$ -Amyloid Aggregation

Simone Brogi,<sup>1,2</sup> Stefania Butini,<sup>1,2</sup> Samuele Maramai,<sup>1,2</sup> Raffaella Colombo,<sup>3</sup> Laura Verga,<sup>4</sup> Cristina Lanni,<sup>3</sup> Ersilia De Lorenzi,<sup>3</sup> Stefania Lamponi,<sup>1,2</sup> Marco Andreassi,<sup>1,2</sup> Manuela Bartolini,<sup>5</sup> Vincenza Andrisano,<sup>6</sup> Ettore Novellino,<sup>1,7</sup> Giuseppe Campiani,<sup>1,2</sup> Margherita Brindisi<sup>1,2</sup> & Sandra Gemma<sup>1,2</sup>

1 European Research Centre for Drug Discovery and Development (NatSynDrugs), University of Siena, Siena, Italy

2 Dipartimento di Biotecnologie, Chimica e Farmacia, University of Siena, Siena, Italy

3 Dipartimento di Scienze del Farmaco, University of Pavia, Pavia, Italy

4 Department of Pathology, Fondazione IRCCS, Policlinico S. Matteo, University of Pavia, Pavia, Italy

5 Department of Pharmacy and Biotechnology, University of Bologna, Bologna, Italy

6 Department for Life Quality Studies, University of Bologna, Rimini, Italy

7 Dipartimento di Farmacia, University of Napoli Federico II, Napoli, Italy

### Keywords

Alzheimer's disease; Amyloid beta oligomers; Amyloid beta peptides; Cholinesterase inhibitors; Molecular dynamics; Multifunctional ligands.

### Correspondence

Stefania Butini, European Research Centre for Drug Discovery and Development (NatSynDrugs), University of Siena, via Aldo Moro 2, 53100 Siena, Italy.  
Tel.: +0039 0577 234161;  
Fax: +0039 0577 234254;  
E-mail: butini3@unisi.it  
and

Dipartimento di Biotecnologie, Chimica e Farmacia, University of Siena, via Aldo Moro 2, 53100 Siena, Italy

Received 13 February 2014; revision 18 April 2014; accepted 30 April 2014

### SUMMARY

**Aims:** We recently described multifunctional tools (**2a–c**) as potent inhibitors of human Cholinesterases (ChEs) also able to modulate events correlated with  $A\beta$  aggregation. We herein propose a thorough biological and computational analysis aiming at understanding their mechanism of action at the molecular level. **Methods:** We determined the inhibitory potency of **2a–c** on  $A\beta_{1-42}$  self-aggregation, the interference of **2a** with the toxic  $A\beta$  oligomeric species and with the postaggregation states by capillary electrophoresis analysis and transmission electron microscopy. The modulation of  $A\beta$  toxicity was assessed for **2a** and **2b** on human neuroblastoma cells. The key interactions of **2a** with  $A\beta$  and with the  $A\beta$ -preformed fibrils were computationally analyzed. **2a–c** toxicity profile was also assessed (human hepatocytes and mouse fibroblasts). **Results:** Our prototypical pluripotent analogue **2a** interferes with  $A\beta$  oligomerization process thus reducing  $A\beta$  oligomers-mediated toxicity in human neuroblastoma cells. **2a** also disrupts preformed fibrils. Computational studies highlighted the bases governing the diversified activities of **2a**. **Conclusion:** Converging analytical, biological, and *in silico* data explained the mechanism of action of **2a** on  $A\beta_{1-42}$  oligomers formation and against  $A\beta$ -preformed fibrils. This evidence, combined with toxicity data, will orient the future design of safer analogues.

doi: 10.1111/cns.12290

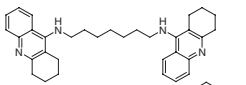
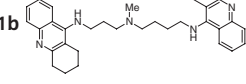
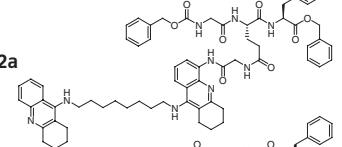
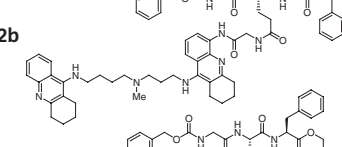
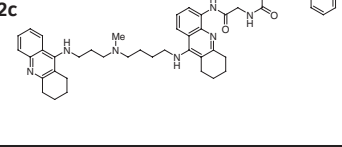
### Introduction

Alzheimer's disease (AD) is a multifactorial and fatal neurodegenerative disorder characterized by the neuropathological extracellular accumulation of  $A\beta$  plaques and the intracellular accumulation of hyperphosphorylated tau protein in the form of neurofibrillary tangles. Currently available therapies for AD only treat disease symptoms and do not address the underlying disease processes [1], thus making AD as the biggest unmet medical need in neurology. As age is the major risk factor, AD has become an urgent public health problem being projected to lead to epidemic levels unless a disease-modifying anti-Alzheimer's drug (DMAAD)

can be found [2]. Although the molecular mechanisms of AD pathogenesis have not been clearly understood, due to its complexity, the use of acetylcholinesterase (AChE) and butyrylcholinesterase (BuChE) inhibitors represents the only therapeutic approach to the disease. Cholinesterase (ChE) inhibitors of catalysis apparently improve cognitive functions and do not have profound disease-modifying effects [3–5], although AChE also accelerates the assembly of  $A\beta$  to amyloid fibrils [6].

The formation of  $A\beta$  deposits in the brain is a seminal step in the development of AD [7], and inhibiting  $A\beta$  oligomerization can provide a novel approach for treating the underlying cause of AD. Recent advances have indeed demonstrated the pathological

**Table 1** Inhibition of human cholinesterases activities, A $\beta_{1-42}$  spontaneous and human AChE-induced A $\beta_{1-40}$  aggregation by compounds **1a,b** and **2a-c**

Compounds structure and number	$K_i$ (nM) hAChE <sup>a</sup>	$K_i$ (nM) hBuChE <sup>a</sup>	IC <sub>50</sub> ( $\mu$ M) A $\beta_{1-42}$ aggreg. <sup>b</sup>	A $\beta_{1-40}$ hAChE-induced aggreg. (%)
<b>1a</b> 			8.3 <sup>c</sup>	68 <sup>d</sup>
<b>1b</b> 	0.012	0.82	55.5	50 <sup>a</sup>
<b>2a</b> 	1.92	49.8	58.9	26 <sup>a</sup>
<b>2b</b> 	5.02	61.77	82.2 <sup>e</sup>	42 <sup>a</sup>
<b>2c</b> 	1.48	21.26	51.0 <sup>a</sup>	42 <sup>a</sup>

<sup>a</sup>Data from reference [11]. <sup>b</sup>A $\beta_{1-42}$  = 50  $\mu$ M; data are the mean of two independent measurements made in duplicate; standard error of the mean (SEM) were within 10%; Tacrine does not significantly inhibit amyloid aggregation when tested at 50  $\mu$ M. <sup>c</sup>Reference [12]. <sup>d</sup>Reference [8]. <sup>e</sup>Datum extrapolated (the full inhibition curve could not be achieved).

assembly of A $\beta$  as a causal factor in AD, and disease progression has been shown to closely correlate with the level of soluble A $\beta$  oligomers. Prefibrillar, soluble oligomers of A $\beta$  have been indicated as the early and key intermediates in AD-related synaptic dysfunction [7].

The multifactorial nature of AD supports the current innovative therapeutic approach of multitarget directed ligands (MTDLs) [8]. Based on preliminary data on bis-tacrine ChE inhibitors (**1a** [9], **1b** [10], Table 1), and to facilitate the identification of effective DMAADs, we recently described appropriately functionalized bis-tacrine compounds as new pharmacological tools (**2a-c**, Table 1) [11] able to interfere with both spontaneous and induced A $\beta$  aggregation while retaining potent antienzymatic (catalytic) properties (Table 1 second and third column).

We herein propose a thorough investigation of the additional effect displayed by our prototypical multipotent compound **2a**. Inhibition of spontaneous A $\beta$  oligomerization process and disruption of the preformed fibrils induced by **2a** and its analogues have been more in depth analyzed by combining *in vitro* aggregation experiments with cellular studies on human neuroblastoma cells (Table 1 and Figures 1 and 2) and with computational approaches (Figures 3 and 4). In particular, we hypothesized the binding mode of **2a** with A $\beta_{1-42}$  and its interactions with the fibrils.

Furthermore, we have analyzed, in comparison with tacrine (a drug recently discontinued in US due to its documented hepatotoxicity) [15], the toxicity profile of **2a-c** in human fibroblast and hepatocytes (Table 2).

All these data will be crucial for driving the rational design of analogues characterized by improved druggability.

## Methods

### Determination of the Inhibitory Potency on A $\beta_{1-42}$ Self-Aggregation

Procedure concerning the determination of the inhibitory potency of the presented compounds (Table 1) on A $\beta_{1-42}$  self-aggregation is described in the Supporting Information.

### Capillary Electrophoresis (CE) and Transmission Electron Microscopy (TEM)

Experimental procedures were performed as already reported [11]. Details are provided in the Supporting Information.

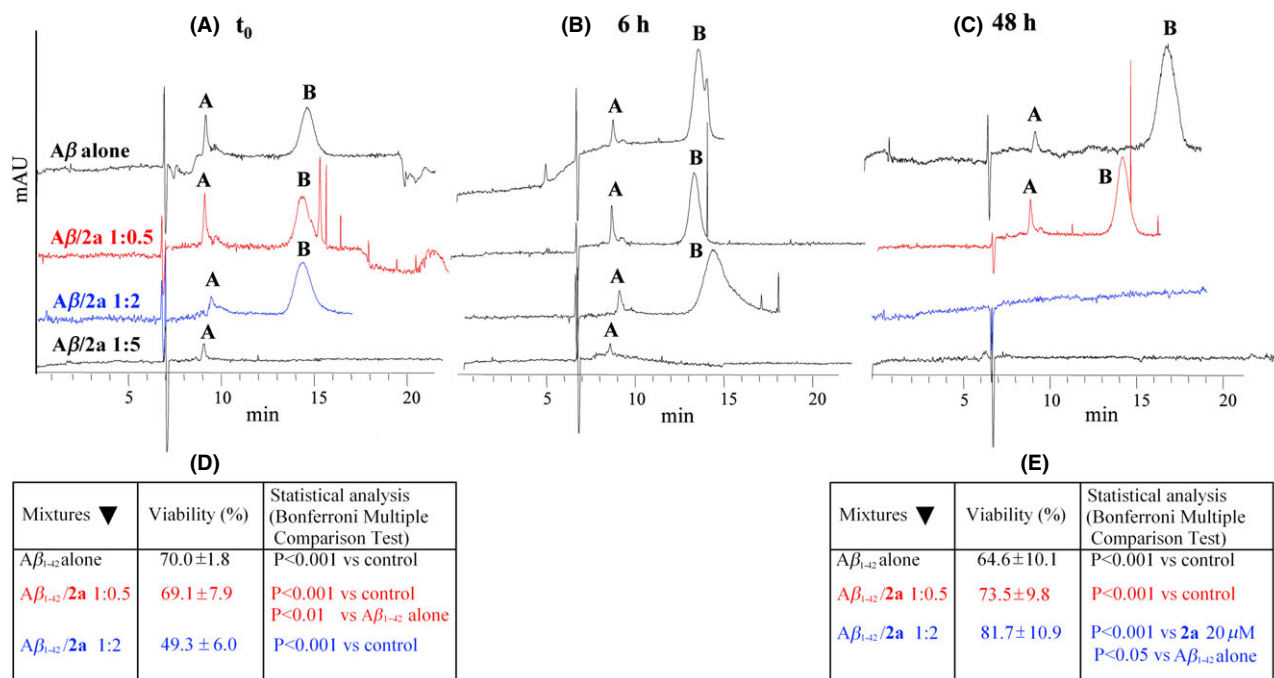


**Figure 1** (A–C) Monitoring of  $A\beta_{1-42}$  (100  $\mu$ M) aggregation by capillary electrophoresis, in absence and presence of increasing concentrations of compound **2a** (from top to bottom) and at increasing elapsed time from co-incubation (from panel A to panel C); (D) cell viability on SH-SY5Y neuroblastoma cells expressed as % of untreated cells for 10  $\mu$ M  $A\beta_{1-42}$  alone and 10  $\mu$ M  $A\beta_{1-42}$  co-incubated with increasing concentrations of **2a**, at  $t_0$  (immediately after solubilization), and (E) at  $t$  48 h (48 h after solubilization). In C–D panels, data are normalized as % control (1.5% ethanol in phosphate buffer).

### Evaluation of $A\beta_{1-42}$ Toxicity Modulation by **2a** and **2b** in Human Neuroblastoma Cells

The assays were performed by means of a 3-(4,5-dimethylthiazol-2-yl)-2,5-diphenyl-tetrazolium bromide (MTT) colorimetric assay on a human neuroblastoma SH-SY5Y cells. Experimental details are provided in the Supporting Information.

### Computational Procedure

Computational procedures based on molecular docking studies coupled to molecular dynamics (MD) simulation were carried out as reported [16–18]. Molecular modeling details are provided in the Supporting Information.

### Cellular Toxicity Evaluation

The cytotoxicity assays were performed on the NIH3T3 and WRL-68 cells as described [17–20]. Further details are provided in the Supporting Information.

## Results

With the aim of elucidating the mechanism of action of our identified tools, we have investigated compounds **2a–c** for better studying their interference with spontaneous  $A\beta_{1-42}$  self-oligomerization process and with  $A\beta_{1-42}$  pre- and postaggregation states.

### Evaluation of the Inhibitory Potency on $A\beta_{1-42}$ Self-Aggregation

To complete the panel of information relative to the inhibitory potency of compounds **2a–c** on  $A\beta_{1-42}$  spontaneous aggregation, and as the  $IC_{50}$  value was previously determined only for **2b**, a reinvestigation was performed by determining the  $IC_{50}$  for the other analogues (using a Thioflavin T-based fluorometric assay). The full profile of the compounds is given in Table 1, where old data relative to the inhibition of  $hChEs$  ( $K_i$  values) and the  $hAChE$ -induced  $A\beta_{1-40}$  aggregation are listed together with the new data. Although less potent than the bis-tacrine analogue **1a**, compounds **2a–c** behave as two-digit  $\mu$ M inhibitors of  $A\beta$  self-aggregation and are characterized by similar potency.

### Effect of Compound **2a** on Pre-Aggregation State of $A\beta_{1-42}$ : CE Studies

The CE method enables a qualitative analysis over time of the oligomers formed along the fibrillogenesis process of  $A\beta_{1-42}$  by the separation of the multimeric fraction responsible for  $A\beta_{1-42}$  toxicity (peak B) from smaller oligomers (peak A) [11,21,22]. This analysis can be performed also in the presence of small molecules, starting from their co-solubilization with the peptide sample ( $t_0$ ).

In Figure 1 (panels A–C),  $A\beta_{1-42}$  alone shows over time an increase of peak B at the expenses of peak A (not-toxic oligomers). A quantitative evaluation of the oligomer peak areas is intrinsically inaccessible, as in the absence of standards a proper

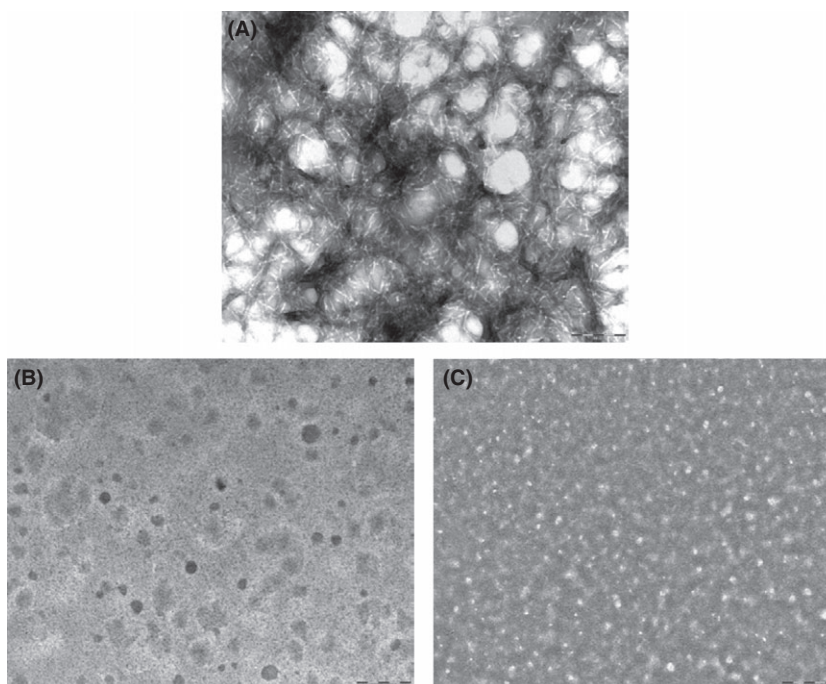


**Figure 2** Transmission electron microscopy images: (A) 100  $\mu\text{M}$   $A\beta_{1-42}$ ; (B) 100  $\mu\text{M}$   $A\beta_{1-42}$  co-incubated with **2a** (50  $\mu\text{M}$ ); (C) preformed  $A\beta_{1-42}$  fibrils after incubation with **2a** (50  $\mu\text{M}$ ). Images are taken at  $t = 5$  day and are representative of those obtained for each of at least two replicates. Scale bar: 200 nm, magnification 60,000x.

calibration curve cannot be built up. However, a semi-quantitative analysis of the area percentages is possible (Figure S1). Ultrafiltration experiments and CE analysis of the filtered and the retained solutions have previously suggested that a conversion from smaller (trimers  $\leq$  peak A  $\leq$  undecamers) to larger (peak B  $>22$ mers) oligomers occurs [11]. Following co-incubation, compound **2a** exhibits a concentration-dependent effect on the formation of  $A\beta_{1-42}$  toxic multimers. In detail, at lower concentrations of compound (50  $\mu\text{M}$ ,  $A\beta_{1-42}/\mathbf{2a}$  1:0.5) the growth of toxic oligomers is stabilized, while at higher concentrations a slow (200  $\mu\text{M}$ ,  $A\beta_{1-42}/\mathbf{2a}$  1:2, 48 h) or fast (500  $\mu\text{M}$ ,  $A\beta_{1-42}/\mathbf{2a}$  1:5  $t_0$ ) oligomer depletion is induced. Notably, oligomer depletion nicely correlates with lower toxicity on SH-SY5Y cells, as explained below.

### Effect of Compounds **2a** and **2b** on Preaggregation State of $A\beta_{1-42}$ : Viability Studies on SH-SY5Y Neuroblastoma Cells

In line with the CE data and to investigate the toxicity of the  $A\beta$  aggregates formed after co-incubation with tested compounds, we have performed cell viability studies on SH-SY5Y neuroblastoma cells. Preliminary cell viability tests, at different concentration of **2a,b**, demonstrated a comparable toxicity profile for these analogues (see Table S1A, **2a** 5  $\mu\text{M}$  = 61.7 vs. **2b** 5  $\mu\text{M}$  = 78.4, and **2a** 20  $\mu\text{M}$  = 40.5 vs. **2b** 20  $\mu\text{M}$  = 49.9, as viability %). In compliance with CE experiments, we have tested SH-SY5Y neuroblastoma cells viability in the presence of  $A\beta_{1-42}$  alone and of  $A\beta_{1-42}$  mixed with the compounds in 1:0.5 and 1:2 ratios. In line with CE data, where at  $t_0$  peak B (toxic oligomers) is still detectable (Figure 1A red and blue traces), a comparable cell toxicity was found for  $A\beta_{1-42}$  alone and for  $A\beta_{1-42}$  mixed with **2a** in 1:0.5 ratio (Figure 1D, red row). The same effect was also observed with **2b**

( $A\beta_{1-42}/\mathbf{2b}$  1:0.5; 75% viability, Table S1B). Increasing the compound doses, in line with the intrinsic toxicity profile of the same, a decrease in viability was observed (Figure 1D blue row for **2a** and Table S1B for **2b**:  $A\beta_{1-42}/\mathbf{2b}$  1:2; 54.7% viability). Further, for tracing out the CE outcome where peak B was still present after 48 h of co-incubation with  $A\beta_{1-42}/\mathbf{2a}$  1:0.5 (Figure 1C, red trace) and absent with  $A\beta_{1-42}/\mathbf{2a}$  1:2 (Figure 1C, blue trace), **2a** was co-incubated with  $A\beta_{1-42}$  for 48 h and the cells were then treated with the resulting amorphous aggregates (Figure 1E, blue and red rows). Cell viability at 5  $\mu\text{M}$  **2a** (Figure 1E, red row) is unvaried and underwent a significant rise at 20  $\mu\text{M}$  **2a** (Figure 1E, blue row), thus indicating an overall toxicity lowering. These data are consistent with CE results which clearly evidence the capability of **2a**, at 200  $\mu\text{M}$  and in 48 h, in lowering toxic oligomers content, thus leading to the formation of amorphous aggregates, as evidenced from TEM results [11]. Notably, the preincubated mixture is less toxic than  $A\beta_{1-42}$  alone or **2a** alone and also of their mixture at  $t_0$ . Collectively, the data obtained with our lead **2a** represent the proof-of-concept for the original hypothesis, which inspired the development of this class of multifunctional compounds.

### Effect of Compound **2a** on Postaggregation State of $A\beta_{1-42}$ : TEM Data

#### $A\beta_{1-42}$ Fibrillogenesis Inhibition

As shown in Figure 2A, the control experiment, with  $A\beta$  peptide alone, exhibits typical nonbranching fibrils. The incubation of higher concentrations of **2a** (i.e., 200 and 500  $\mu\text{M}$ ) has shown the absence of fibrils at TEM inspection [11]. The amorphous aggregates of Figure 2B further show that this is the case also when a lower concentration (50  $\mu\text{M}$ ) of **2a** was added. Taken altogether,



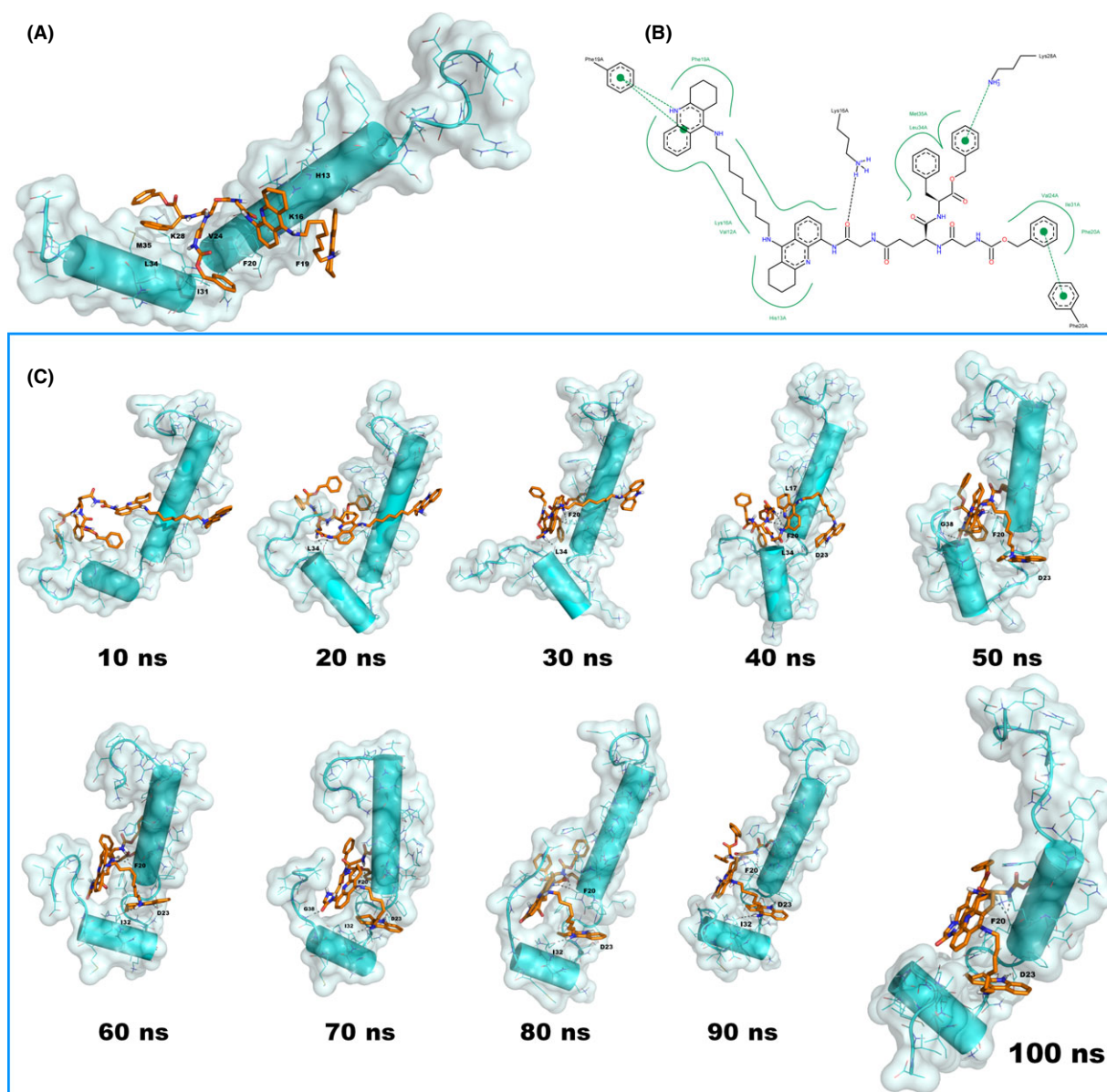


**Figure 3** (A) Best docked pose of **2a** (orange stick) in complex with Aβ<sub>1-42</sub> (cyan cartoon). H-bonds are reported by gray dotted lines, the picture was generated by means of PyMOL [13], the nonpolar hydrogen atoms are omitted for the sake of clarity; (B) schematic representation of the interactions based on docking calculation. The H-bonds are reported as black dotted lines while the π-π or cation-π stacking are reported as green dotted lines. The picture was generated by means of PoseView [14]; (C) **2a** (orange stick) and Aβ<sub>1-42</sub> peptide (cyan cartoon) complex: progression of MD simulation. The picture was generated by means of PyMOL [13], the nonpolar hydrogen atoms are omitted for the sake of clarity.

the CE and TEM data make us reasonably conclude that either the stabilization (induced by the addition of 50 μM **2a**) or the disaggregation (induced by the addition of 200 or 500 μM **2a**) of toxic peak B (Figure 1C) correspond to a clear antifibrillogenic activity.

#### Aβ<sub>1-42</sub> Preformed Fibrils Disaggregation

Five days after solubilization in an aqueous medium is an adequate time window for Aβ<sub>1-42</sub> to grow classical mature fibrils, analogous to those shown in Figure 2A. Interestingly, the *in vitro* antiamyloid activity of compound **2a** also applies to preformed

fibrils, at all concentrations tested. The amorphous aggregates evident in Figure 2C are representative of the disaggregation effect of **2a** at a concentration as low as 50 μM.

#### *In Silico* Studies of the Effect of Multifunctional AChE Modulator on Pre- and Postaggregation States of Aβ<sub>1-42</sub>

*In silico* studies (molecular docking coupled to a MD simulation protocol) have been performed on **2a** as the better characterized of our ligands both *in vitro* (fibrillogenesis, CE and TEM) and in

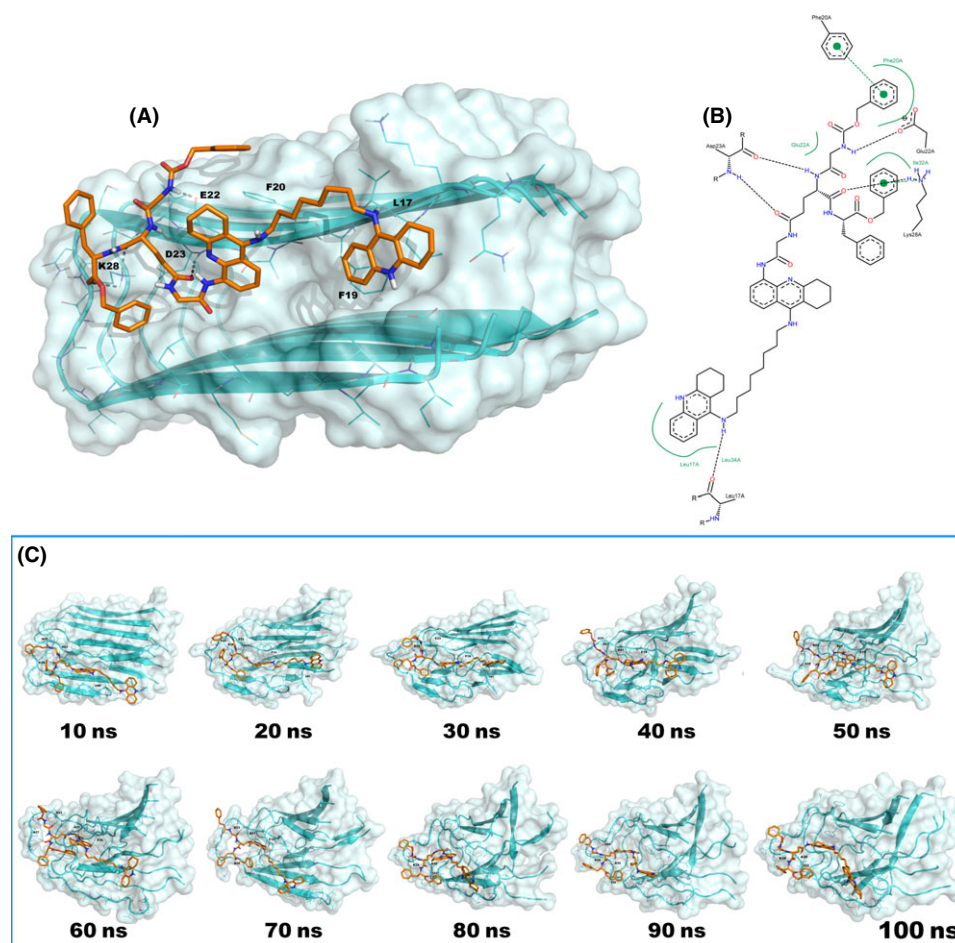


**Figure 4** (A) Best docked pose of **2a** (orange stick) in complex with Aβ<sub>1-42</sub> fibrils (cyan cartoon). H-bonds are reported by gray dotted lines, the picture was generated by means of PyMOL [13], the nonpolar hydrogen atoms are omitted for the sake of clarity; (B) schematic representation of the interactions based on docking calculation. The H-bonds are reported as black dotted lines while the π-π or cation-π stacking are reported as green dotted lines. The picture was generated by means of PoseView PyMOL [14]; (C) **2a** (orange stick) and fibrils form Aβ<sub>1-42</sub> (cyan cartoon) complex: progression of MD simulation. The picture was generated by means of PyMOL [13], the nonpolar hydrogen atoms are omitted for the sake of clarity.

cellular studies. The aim of the computational analysis was to understand at the molecular level the experimentally determined effects of the multifunctional compound **2a**: (i) the prevention of Aβ<sub>1-42</sub> self-aggregation and (ii) the disaggregation effect on the preformed fibrils.

### Effect of Compound **2a** on Preaggregation State of Aβ<sub>1-42</sub>: Computational Studies

To rationalize the experimental data related to the potency of **2a** in the inhibition of Aβ<sub>1-42</sub> peptide aggregation (Table 1) and in prevention of the misfolding event of amyloid leading to oligomerization (CE studies), intensive modeling studies were performed by using the crystal structure of Aβ<sub>1-42</sub> (PDB ID: 1IYT [23]) and applying molecular docking and MD techniques as reported in literature [24–26]. Our docking protocol employed GOLD software [27] using the scoring function GoldScore [28]. The output (Figure 3) is referred to the most populated cluster found by docking. **2a** strongly interacts by its bis-tacrine system

with H13 (hydrophobic contacts) and P19 by a π-π stacking, while the peptide portion of the molecule forms a H-bond with K16, a cation-π stacking with K28 by the benzyl ester function and a π-π stacking with F20 by the benzyl carbamate (Figure 3B). Our findings are in agreement with data recently obtained by others [24]. The high GoldScore (83.59) and the favorable free-binding energy (Prime MM/GBSA [29], ΔG<sub>bind</sub> = -115.65 kcal/mol) indicate a high affinity of **2a** for the monomeric peptide.

Starting from the docking pose (Figure 3A), we performed MD simulation (Desmond) [30,31] in water. Essentially, the trajectory of the MD simulation confirms the docking results. In fact, as observed in Figure 3C, the position of **2a** is maintained between the central hydrophobic region and C-terminal region of Aβ<sub>1-42</sub>. The protonated terminal tacrine moiety initially lacks the contact with F19, forming a H-bond with D23 and I32. These latter polar contacts maintain the protonated tacrine moiety in the same position for all the simulation thus allowing it to re-establish a contact with F19. On the other hand, the peptide-bound tacrine replaces the hydrophobic contact with H13 with a more favorable π-π

**Table 2** Cytotoxic effect on the NIH3T3 and human liver embryo WRL-68 cell lines. Cell viability after 24 h of incubation was measured by the Neutral Red Uptake (NRU) test and data normalized as % control (Polystyrene)<sup>a</sup>

Tested doses ►					
Cmpds					
▼	1 μM	10 μM	30 μM	100 μM	300 μM
NIH3T3 cells					
Tacrine	98 ± 3	94 ± 6	83 ± 2*	52 ± 4*	26 ± 5*
<b>2a</b>	93 ± 4	30 ± 6*	18 ± 4*	0	0
<b>2b</b>	103 ± 6	95 ± 5*	91 ± 4*	72 ± 7*	54 ± 6*
<b>2c</b>	97 ± 4	91 ± 3*	89 ± 4*	71 ± 6*	0
WRL-68 cells					
Tacrine	56 ± 4*	41 ± 2*	39 ± 2*	37 ± 2*	17 ± 1*
<b>2a</b>	33 ± 3*	33 ± 2*	32 ± 4*	20 ± 6*	14 ± 2*
<b>2b</b>	56 ± 3*	48 ± 2*	42 ± 2*	40 ± 1*	38 ± 5*
<b>2c</b>	54 ± 5*	38 ± 2*	34 ± 2*	23 ± 6*	13 ± 2*

<sup>a</sup>Data are expressed as mean ± SD of three experiments repeated in six replicates. All compounds were tested at increasing concentrations ranging from 1 to 300 μM. \*Values are statistically different versus control,  $P \leq 0.05$ .

stacking with F20, which will persist for all the simulation. The peptide moiety preserves, although occasionally, the cation- $\pi$  stacking with K28, while it is involved in a strong H-bond network with the backbones of F20, G38, and L34. Notably, the analysis of the MD trajectory (PoseView [14]) revealed hydrophobic contacts for the benzyl carbamate moiety with M35, L17, and A21, residues which are constantly targeted during the simulation. The benzyl ester group is mainly involved in hydrophobic contacts with V24, V39, V40, and I41. These findings support a high affinity of **2a** for  $A\beta_{1-42}$  monomer and help in explaining its mechanism of action. In fact, **2a** could prevent the misfolding of the C-terminal region to  $\beta$ -sheet, as during the 100 ns no change of secondary structure is observed (Figure 3) and the helix is constantly conserved. Concerning the amino-acids of  $A\beta_{1-42}$ , their fluctuation plot (Figure S2) confirms the overall stability of the structure. In fact, as expected, only a restricted number of residues at the N- and at the C-terminal ends show a relevant difference in root mean square fluctuation (RMSF), whereas for all the other residues no evident fluctuation is observed, in line with the evidence that the secondary structure appears stabilized. It is notable that the misfolding event at the C-terminal end of  $A\beta_{1-42}$  alone has been observed [32] already after 20 ns of simulation in water. Furthermore, based on a recently published model [33], the misfolded C-terminal region ( $\beta$ -hairpin) folds up toward the central hydrophobic region, thus triggering the step that drives to oligomerization. As observed in our calculations, **2a** could physically prevent this type of arrangement, as it lies between the above-mentioned key regions and does not allow the misfolding of  $A\beta_{1-42}$ .

In conclusion, our molecular docking and MD simulations demonstrated that **2a** strongly binds to  $A\beta_{1-42}$  and intensely interacts with the key regions of the  $\alpha$ -helical conformation of the peptide, thus leading to its stabilization. This event may reduce the potential interaction with other  $A\beta_{1-42}$  monomers by preventing the

folding of the C-terminal region from helix to  $\beta$ -sheet that has been identified as key step in the oligomerization process [34,35].

The mechanism of action proposed for **2a** is in line with CE and cellular studies (Figure 1). It is plausible that a similar mechanism could govern the activity of its structurally related analogues **2b,c**, which displayed an antifibrillogenic activity comparable to that of **2a** (Table 1).

### Effect of Compound 2a on Postaggregation State of $A\beta_{1-42}$ : Computational Studies

The observation by TEM analysis that **2a** is able to disaggregate preformed fibrils of  $A\beta_{1-42}$  after incubation of these latter with 50 (Figure 2C), 200 or 500 μM [11], prompted us to explain this event by applying to the fibrils the same protocol used for the  $A\beta_{1-42}$  peptide. Molecular docking and/or MD protocols have been widely applied for observing and rationalizing the mechanism of action of different classes of compounds in fibrils disruption [36–42]. The structure of the  $A\beta_{1-42}$  fibrils was found in the PDB (PDB ID: 2BEG [43]) and was managed as described [42,44]. In each peptide chain, the residues Q15-K16 were added to the model in an extended conformation to ensure the  $\beta$ -sheet complementarity of the U-shaped pentamer [42,44]. The resulting structure was then used for our computational studies.

Docking calculation (Figure 4A) performed by means of GOLD software [27] revealed that the best cluster of docked solutions establishes a relevant number of polar contacts with key residues of the fibril complex. In fact, the protonated tacrine moiety is able to interact with L17 of chain A, while the tacrine bringing the peptide lies in proximity of the F19 of the same chain (Figure 4A). The peptide moiety interacts with chain A residues E22 and D23 by polar contacts and in particular with K28 by a cation- $\pi$  stacking with the benzyl ester (Figure 4B), while the benzyl carbamate establishes a  $\pi$ - $\pi$  stacking with F20 (chain A). It is noticeable that the targeted residues are widely accepted as pivotal for stabilizing and aggregating the fibrils. In fact, the hydrophobic central region L17-E22 is involved in fibrils assembly [42,44,45], while the residues D23 and K28 are involved in a salt bridge that is necessary for the fibrils stability [42,44,45]. Interestingly, the formation of H-bonds between **2a** and K28 and/or D23 may not be favorable to the formation of the mentioned salt bridge. The docking score value of 67.71 and the favorable estimated free-binding energy (Prime MM/GBSA [29],  $\Delta G_{\text{bind}} = -162.03$  kcal/mol) confirm the significant affinity of **2a** for the  $A\beta$  fibrils. Relevantly, our MD simulation study performed using Desmond software [30,31] is in agreement with the outcome obtained from the docking calculation. Accordingly, during 100 ns of MD simulation, **2a** maintains the previously described contacts and strongly interacts with the fibrils (PoseView [14]). Initially, F20 stacks with the benzyl carbamate, but a more favorable  $\pi$ - $\pi$  stacking with the peptide-bound tacrine was observed already after 10 ns (Figure 4C). In fact, during the simulation, the benzyl carbamate moiety is principally involved in H-bonds with K28 and/or D23 and not seldom with E22, V24 (hydrophobic contacts), G25, and S26. The benzyl ester is frequently involved in H-bonds with N27, A30, I32 from chain A and L34 (chain B). Interestingly, the protonated tacrine forms H-bond with I41 and the carbon linker of **2a** establishes a series of hydrophobic contacts with L34 (chains A, B, C), V36 (chain B),



V39, and V40 (chains A, B, C). The central tacrine is constantly involved in H-bond with F19 backbone and establishes hydrophobic contacts with L17, F19 (frequently by  $\pi$ - $\pi$  stacking), F20, V40 of chain A. Notably, after about 40 ns of MD, the  $A\beta$  fibrils lack the ordered organization and disruption starts (Figure 4C).

At the end of the 100 ns of the MD simulation, the disordered state of the  $A\beta$  fibrils complex is largely evident (as they lack the predominant contacts necessary for stabilizing the structure). For example, the salt bridge between D23 and K28 is totally removed by the interaction with **2a** (K28 and/or D23 are targeted during all the simulation) as the distance between these residues is increased and is not compatible with any polar contact (Figure S3). A big amount of intramolecular H-bonds between the  $\beta$ -sheets backbone that stabilize the overall structure are also sensibly reduced by the interaction with **2a**. This event leads to an increase of RMSF proportional to destabilization of the structure (Figure S4). Moreover, the distances between the residues from the same fibrils also undergo a dramatic change, further contributing to the disruption of the  $A\beta$  fibrils assembly. In fact, as reported in Figure S5, the distances measured between selected residues (A21 from chain A with V36 chain A and V36 chain B) during simulation display very large differences between the starting structure and the structure at the end of the MD (e. g. the distance of A21 and V36A and V36B measures 9.4 Å and 6.2 Å, respectively, at the beginning, while at the end the MD it becomes of 23.6 Å and 20.7 Å, Figure S6).

Summing up, the computational procedure herein discussed provided the explanation of the biological events encountered with **2a** binding the peptide  $A\beta_{1-42}$  (that ultimately inhibits oligomer formation and fibrillization), as well as its role in promoting  $A\beta$  fibrils disruption. These data confirm the reliability of the computational approaches for investigating complex molecular mechanisms that to date can hardly be studied experimentally (in solution).

### Toxicity Studies on NIH3T3 and WRL-68 Cells

Cytotoxicity assays were performed to establish the effect of compounds **2a–c** on the mouse fibroblasts NIH3T3 cells and on the human liver embryo WRL-68 cell line (Table 2).

Cytotoxicity data for the NIH3T3 cells demonstrate that tacrine, at low doses (1  $\mu$ M), has almost no toxicity. Afterward, toxicity dose-dependently increases for tacrine and **2a** (being this latter more toxic than the reference tacrine). On the contrary, analogues **2b,c** did not show relevant toxicity on these cells up to

100  $\mu$ M. In the same test, **2b** showed the best profile among the tested compounds.

Moreover, in line with the hepatotoxicity of tacrine [15], the toxicity potential of **2a–c** on the human liver embryo WRL-68 cells was assessed. The results evidence that **2a** was more toxic than tacrine already at 1  $\mu$ M, while **2b,c** displayed comparable or lower toxicity with respect to tacrine. Again, **2b** shows the best profile within the series. These data might be ascribable to the presence of a protonatable N in the spacer, which may account for a lower cell permeability of **2b,c**. However, the anti-ChE activity of **2a–c** is in the low nM range (Table 1), whereas comparing anti-fibrillogenic activity ( $IC_{50}$   $A\beta_{1-42}$  aggregation between 51 and 82  $\mu$ M, Table 1) with NIH3T3 toxicity (detectable from 30 to 300  $\mu$ M, Table 2), we could identify a narrow therapeutic window for all three compounds **2a–c**. Toxicity data, although not favorable on hepatic cells, combined with the  $IC_{50}$  values justified further evaluation on human neuronal cells to assess their potential neuroprotective effect against  $A\beta$ -mediated neurotoxicity. Accordingly, we selected **2a** as the most studied analogue, and **2b** as the least toxic of the series. As shown in Figure 1 D–E and Table S1, **2a** demonstrated potential neuroprotective activity at 20  $\mu$ M.

Taken together, toxicity data suggest that the acridine system of **2a–c** should be replaced to allow the development of multipotent compounds with limited hepatotoxicity.

### Conclusion

Combination of biological data and *in silico* data led to the explanation of the mechanism governing the activity of **2a** on  $A\beta$  oligomers formation and against the  $A\beta_{1-42}$  preformed fibrils. Studies on human neuroblastoma cells confirmed the potential neuroprotective role of the lead compound **2a**. Furthermore, the definition of the molecular basis of the interaction with  $A\beta$  combined to the evaluation of the  $A\beta$ -mediated toxicity profile highlighted the possibility of developing multipotent compounds with acceptable safety.

### Acknowledgment

The authors thank COST CM1103, BioSolveIT GmbH for providing academic license of PoseView.

### Conflict of Interest

The authors declare no competing financial interests.

### References

- Sadowski M, Wisniewski T. Disease modifying approaches for Alzheimer's pathology. *Curr Pharm Des* 2007;**13**:1943–1954.
- Mount C, Downton C. Alzheimer disease: Progress or profit? *Nat Med* 2006;**12**:780–784.
- McShane R, Areosa SA, Minakaran N, Memantine for dementia. *Cochrane Database Syst Rev* 2006; CD003154.
- Cummings JL. Treatment of Alzheimer's disease: Current and future therapeutic approaches. *Rev Neurol Dis* 2004;**1**:60–69.
- Standridge JB. Pharmacotherapeutic approaches to the prevention of Alzheimer's disease. *Am J Geriatr Pharmacother* 2004;**2**:119–132.
- Alvarez A, Opazo C, Alarcon R, Garrido J, Inestrosa NC. Acetylcholinesterase promotes the aggregation of amyloid-beta-peptide fragments by forming a complex with the growing fibrils. *J Mol Biol* 1997;**272**:348–361.
- Lauren J, Gimbel DA, Nygaard HB, Gilbert JW, Strittmatter SM. Cellular prion protein mediates impairment of synaptic plasticity by amyloid-beta oligomers. *Nature* 2009;**457**:1128–1132.
- Bolognesi ML, Cavalli A, Valgimigli L, et al. Multi-target-directed drug design strategy: From a dual binding site acetylcholinesterase inhibitor to a trifunctional compound against Alzheimer's disease. *J Med Chem* 2007;**50**:6446–6449.
- Pang YP, Quiram P, Jelacic T, Hong F, Brimijoin S. Highly potent, selective, and low cost bis-tetrahydroaminacrine inhibitors of acetylcholinesterase. Steps toward novel drugs for treating Alzheimer's disease. *J Biol Chem* 1996;**271**:23646–23649.
- Butini S, Campiani G, Borriello M, et al. Exploiting protein fluctuations at the active-site gorge of human cholinesterases: Further optimization of the design strategy to develop extremely potent inhibitors. *J Med Chem* 2008;**51**:3154–3170.



11. Butini S, Brindisi M, Brogi S, et al. Multifunctional cholinesterase amyloid beta fibrillization modulators. Synthesis and biological investigation. *ACS Med Chem Lett* 2013;**4**:1178–1182.
12. Minarini A, Milelli A, Tumiatti V, et al. Cystamine-tacrine dimer: A new multi-target-directed ligand as potential therapeutic agent for Alzheimer's disease treatment. *Neuropharmacology* 2012;**62**:997–1003.
13. The PyMOL molecular graphics system, version 1.6.alpha. New York: Schrödinger, LLC, 2013.
14. Stierand K, Rarey M. Consistent two-dimensional visualization of protein-ligand complex series. *J Cheminform* 2011;**3**:21.
15. Lagadic-Gossmann D, Rissel M, Le Bot MA, Guillozo A. Toxic effects of tacrine on primary hepatocytes and liver epithelial cells in culture. *Cell Biol Toxicol* 1998;**14**:361–373.
16. Anzini M, Di Capua A, Valenti S, et al. Novel analgesic/anti-inflammatory agents: 1,5-diarylpyrrole nitrooxyalkyl ethers and related compounds as cyclooxygenase-2 inhibiting nitric oxide donors. *J Med Chem* 2013;**56**:3191–3206.
17. Cappelli A, Manini M, Valenti S, et al. Synthesis and structure-activity relationship studies in serotonin 5-HT (1A) receptor agonists based on fused pyrrolidone scaffolds. *Eur J Med Chem* 2013;**63**:85–94.
18. Gemma S, Camodeca C, Brindisi M, et al. Mimicking the intramolecular hydrogen bond: Synthesis, biological evaluation, and molecular modeling of benzoxazines and quinazolines as potential antimalarial agents. *J Med Chem* 2012;**55**:10387–10404.
19. Butini S, Gemma S, Brindisi M, et al. Non-nucleoside inhibitors of human adenosine kinase: Synthesis, molecular modeling, and biological studies. *J Med Chem* 2011;**54**:1401–1420.
20. Gemma S, Brogi S, Patil PR, et al. From (+)-epigallocatechin gallate to a simplified synthetic analogue as a cytoadherence inhibitor for *P. falciparum*. *RSC Adv* 2014;**4**:4769–4781.
21. Sabella S, Quaglia M, Lanni C, et al. Capillary electrophoresis studies on the aggregation process of beta-amyloid 1-42 and 1-40 peptides. *Electrophoresis* 2004;**25**:3186–3194.
22. Colombo R, Carotti A, Catto M, et al. CE can identify small molecules that selectively target soluble oligomers of amyloid beta protein and display antifibrillogenic activity. *Electrophoresis* 2009;**30**:1418–1429.
23. Crescenzi O, Tomaselli S, Guerrini R, et al. Solution structure of the Alzheimer amyloid beta-peptide (1-42) in an apolar microenvironment. Similarity with a virus fusion domain. *Eur J Biochem* 2002;**269**:5642–5648.
24. Wang Y, Xia Z, Xu JR, et al. Alpha-mangostin, a polyphenolic xanthone derivative from mangosteen, attenuates beta-amyloid oligomers-induced neurotoxicity by inhibiting amyloid aggregation. *Neuropharmacology* 2012;**62**:871–881.
25. Peters C, Fernandez-Perez EJ, Burgos CF, et al. Inhibition of amyloid beta-induced synaptotoxicity by a pentapeptide derived from the glycine zipper region of the neurotoxic peptide. *Neurobiol Aging* 2013;**34**:2805–2814.
26. Yang C, Zhu X, Li J, Shi R. Exploration of the mechanism for LPPFD inhibiting the formation of beta-sheet conformation of A beta(1-42) in water. *J Mol Model* 2010;**16**:813–821.
27. Jones G, Willett P, Glen RC. Molecular recognition of receptor sites using a genetic algorithm with a description of desolvation. *J Mol Biol* 1995;**245**:43–53.
28. Jones G, Willett P, Glen RC, Leach AR, Taylor R. Development and validation of a genetic algorithm for flexible docking. *J Mol Biol* 1997;**267**:727–748.
29. *Prime, version 3.0*. New York: Schrödinger, LLC, 2011.
30. *Desmond molecular dynamics system, version 3.0*. New York, NY: D. E. Shaw Research, 2011.
31. *Maestro-desmond interoperability tools, version 3.0*. New York, NY: Schrödinger, 2011.
32. Yang C, Li J, Li Y, Zhu X. The effect of solvents on the conformations of Amyloid  $\beta$ -peptide (1–42) studied by molecular dynamics simulation. *J Mol Struct* 2009;**895**:1–8.
33. Roychaudhuri R, Yang M, Deshpande A, et al. C-terminal turn stability determines assembly differences between Abeta40 and Abeta42. *J Mol Biol* 2013;**425**:292–308.
34. Streltsov VA, Varghese JN, Masters CL, Nuttall SD. Crystal structure of the amyloid-beta p3 fragment provides a model for oligomer formation in Alzheimer's disease. *J Neurosci* 2011;**31**:1419–1426.
35. Urbanc B, Betnel M, Cruz L, Bitan G, Teplow DB. Elucidation of amyloid beta-protein oligomerization mechanisms: Discrete molecular dynamics study. *J Am Chem Soc* 2010;**132**:4266–4280.
36. Bruce NJ, Chen D, Dastidar SG, et al. Molecular dynamics simulations of Abeta fibril interactions with beta-sheet breaker peptides. *Peptides* 2010;**31**:2100–2108.
37. Sgarbossa A, Monti S, Lenci F, et al. The effects of ferulic acid on beta-amyloid fibrillar structures investigated through experimental and computational techniques. *Biochim Biophys Acta* 2013;**1830**:2924–2937.
38. Chen D, Martin ZS, Soto C, Schein CH. Computational selection of inhibitors of Abeta aggregation and neuronal toxicity. *Bioorg Med Chem* 2009;**17**:5189–5197.
39. Verma S, Singh A, Mishra A. The effect of fulvic acid on pre- and postaggregation state of Abeta(17-42): Molecular dynamics simulation studies. *Biochim Biophys Acta* 2013;**1834**:24–33.
40. Zhao JH, Liu HL, Elumalai P, et al. Molecular modeling to investigate the binding of Congo red toward GNNQQNY protofibril and *in silico* virtual screening for the identification of new aggregation inhibitors. *J Mol Model* 2013;**19**:151–162.
41. Lemkul JA, Bevan DR. Destabilizing Alzheimer's Abeta (42) protofibrils with morin: Mechanistic insights from molecular dynamics simulations. *Biochemistry* 2010;**49**:3935–3946.
42. Hochdorffer K, Marz-Berberich J, Nagel-Steger L, et al. Rational design of beta-sheet ligands against Abeta42-induced toxicity. *J Am Chem Soc* 2011;**133**:4348–4358.
43. Luhrs T, Ritter C, Adrian M, et al. 3D structure of Alzheimer's amyloid-beta(1-42) fibrils. *Proc Natl Acad Sci USA* 2005;**102**:17342–17347.
44. Kassler K, Horn AH, Sticht H. Effect of pathogenic mutations on the structure and dynamics of Alzheimer's A beta 42-amyloid oligomers. *J Mol Model* 2010;**16**:1011–1020.
45. Rosenman DJ, Connors CR, Chen W, Wang C, Garcia AE. Abeta monomers transiently sample oligomer and fibril-like configurations: Ensemble characterization using a combined MD/NMR approach. *J Mol Biol* 2013;**425**:3338–3359.

## Supporting Information

The following supplementary material is available for this article:

**Figure S1.** Plot of peak B normalized area % versus elapsed time from solubilization (each experimental point is in triplicate).

**Figure S2.** (A) Root mean Square deviation (RMSD) of the  $A\beta_{1-42}$  helix backbone. Root mean square deviation was calculated between the final conformation and the starting conformation through the 100 ns MD simulations. (B) RMSF of all residues of the  $A\beta$  helix. The pictures were generated by Simulation Event Analysis implemented in Desmond.

**Figure S3.** Plot for the distance between D23 and K28 from  $A\beta_{1-42}$  fibrils (chain A). The picture was generated by Simulation Event Analysis implemented in Desmond.

**Figure S4.** (A) Root mean square deviation (RMSD) of the  $A\beta$  fibrils backbone. Root mean square deviation were calculated between the final conformation and the starting conformation through the 100 ns MD simulations. (B) RMSF of all residues of the  $A\beta$  fibrils. The pictures were generated by Simulation Event Analysis implemented in Desmond.

**Figure S5.** (A) Plot for the distance between A21 and V36 from  $A\beta$  fibrils (chain A). (B) Plot for the distance between A21 from chain A and V36 from chain B. The pictures were generated by Simulation Event Analysis implemented in Desmond.

**Figure S6.** (A)  $A\beta$  fibrils (cyan cartoon) distances between A21 from chain A and V36 from chain A and B measured before the Molecular Dynamics simulation. The residues are reported as stick. (B)  $A\beta$  fibrils (green cartoon) distances between A21 from chain A and V36 from chain A and B measured after 100 ns of the Molecular Dynamics simulation. The measures are reported in Å, the picture is generated by PyMOL, all the residues with exclusion of those selected (A21 chain A, V36 chain A and B) and nonpolar hydrogen atoms were omitted for the sake of clarity.

**Table S1:** Cell viability on SH-SY5Y neuroblastoma cells expressed as % of untreated cells for (a) different concentrations of **2a** and **2b**, (b) 10  $\mu\text{M}$   $A\beta_{1-42}$  alone and 10  $\mu\text{M}$   $A\beta_{1-42}$  co-incubated with **2a** and **2b**, at  $t_0$  (immediately after solubilization), (c) 10  $\mu\text{M}$   $A\beta_{1-42}$  alone and 10  $\mu\text{M}$   $A\beta_{1-42}$  peptide co-incubated with **2a** at t 48 h (48 h after solubilization). Data are normalized as % control (1.5% ethanol in phosphate buffer).